Title: Nanoparticles targeted to fibroblast activation protein outperform PSMA for MRI delineation of primary prostate tumours

Nicole Dmochowska[a*] PhD, Valentina Milanova[a*] PhD, Ramesh Mukkamala[b] PhD, Kwok Keung Chow[a], Nguyen T.H. Pham[c] PhD, Madduri Srinivasarao[b] PhD, Lisa M. Ebert PhD[d], Timothy Stait-Gardner[e] PhD, Hien Le[f] MBBS, Anil Shetty[g] MD, Melanie Nelson[g] PhD, Philip S. Low[b] PhD, Benjamin Thierry [a] PhD

[a]Future Industries Institute, University of South Australia, Adelaide, South Australia, Australia
[b]Department of Chemistry and Institute for Drug Discovery, Purdue University, West Lafayette, Indiana, United States
[c]Key Centre for Polymers and Colloids, School of Chemistry, The University of Sydney, Sydney, NSW, Australia
[d] Centre for Cancer Biology, University of South Australia and SA Pathology, Adelaide, South Australia, Australia
[e]Nanoscale Organisation and Dynamics Group, Western Sydney University, Sydney, New South Wales, Australia
[f]Department of Radiation Oncology, Royal Adelaide Hospital, Adelaide, SA, Australia
[g]Ferronova Pty Ltd, Mawson Lakes, SA, Australia

Corresponding author: Professor Benjamin Thierry, Bioengineering Lab, Future Industries Institute, MM Building, University of South Australia Mawson Lakes Campus, University Boulevard, Mawson Lakes, South Australia 5095, Australia, email: Benjamin.thierry@unisa.edu.au, telephone +618 830 23689.

Abstract

Accurate and precise delineation of gross tumour volumes remains a barrier to radiotherapy dose escalation and boost dosing in the treatment of solid tumours, such as prostate cancer. Magnetic resonance imaging of tumour molecular targets has the power to enable focal dose boosting, particularly when combined with technological advances such as MRI-LINAC. Fibroblast activation protein (FAP) is a transmembrane protein overexpressed in stromal components of >90% of epithelial carcinomas. Herein we compare targeted MRI of gold standard PSMA with FAP in the delineation of orthotopic tumours in a mouse model of prostate cancer. Control (no ligand), FAP and PSMA-targeting iron oxide nanoparticles were prepared with modification of an MRI agent (FerroTrace). Mice with orthotopic LNCaP tumours underwent T_2-weighted 3D MRI 24 hours after intravenous injection of contrast agents. FAP and PSMA nanoparticles produced contrast enhancement on MRI when compared to control nanoparticles, which was most pronounced on the tumour periphery. FAP-targeted MRI increased the proportion of tumour contrast enhancing black pixels by 13.37% when compared to PSMA. Furthermore, analysis of changes in R2 values between

healthy prostates and LNCaP tumours indicated an increase in contrast enhancing pixels in the tumour border of 15%, when targeting FAP, in contrast to PSMA This study demonstrates preclinical feasibility of PSMA and FAP-targeted MRI which can enable targeted image-guided focal therapy of localized prostate cancer.

Background

Prostate cancer (PCa) is one of the most diagnosed malignancies in men (1) and, owing to its relatively high survival rate and frequent full gland treatment associated morbidity, is the leading cause of treatment–related years lived with disability worldwide. Along with radical prostatectomy, radiotherapy (RT) is a mainstay treatment option for all stages of disease, and is commonly delivered as a uniform dose over the entire prostate gland (2). There is mounting evidence that the risk of biochemical disease recurrence is reduced with dose escalation when greater than 80 Gy, especially in patients with intermediate or high-risk lesions. However, dose intensification of the whole gland is limited by off-target toxicities to adjacent organs at risk including the rectum, urethra, and bladder (3). Following pelvic radiotherapy, up to 30% of patients experience late grade III or IV genitourinary or gastrointestinal toxicities, with persistent long-term negative impacts on quality of life, through both mental and physical wellbeing, largely due to bowel disturbances(4, 5). Although modern RT techniques enable safer and more precise dose delivery to the prostate, treatment-associated morbidity remains a significant concern in the treatment of PCa patients.

PCa is a multifocal disease, often presenting with large primary intraprostatic lesions accompanied by smaller, well defined secondary lesions. Dominant intraprostatic lesions (index lesion) are considered to be the most aggressive, responsible for driving disease progression and prognosis, and are the most common sites of recurrence (6-8). Focal dose escalation RT approaches specifically target index lesions, balancing the risk of recurrence and patient's quality of life. For example, the recently reported FLAME study demonstrated that focal dose escalation under the guidance of multiparametric MRI (mpMRI) could improve biochemical recurrence free survival by 7%, without impacting morbidity and quality of life (9). Early results from a phase II trial investigating MRI-guided focused ultrasound ablation for localized intermediate risk PCa also demonstrated encouraging oncologic and functional outcomes with 93% of patients disease-free at 5 months after treatment (10). In a cohort of low to intermediate risk PCa, gadolinium enhanced MRI-guided focal laser ablation showed promising early oncologic results with 17% of participants requiring additional oncologic treatment after one year of initial treatment, with no significant side effects or impact to quality of life (11).

Target delineation, a key requirement to define gross tumour volumes (GTV) in intraprostatic focal treatment approaches, is commonly referred to as the Achilles' heel of RT. Owing to its superior soft-tissue resolution compared to computed tomography and the ability to acquire non-invasive functional imaging, mpMRI is rapidly becoming a staple tool in guiding PCa RT and more generally focal ablation. Adoption is supported by powerful technological advances such as the integration of MRI with linear accelerators (MRI-LINAC) and MRI-ultrasound (US)

fusion set-ups that streamline intraoperative US image guidance with the resolution of MRI. However, mpMRI only has a moderate inter-rater agreement and is prone to a large false-positive rate and underestimation of tumour margins (12, 13). In addition, target delineation with mpMRI is not trivial, which substantially lengthens MRI-guided RT procedures and may result in greater intrafraction motion. This is further limited by magnet strength and experience of the imaging team.

A recent study demonstrated increased consensus of prostate specific membrane antigen (PSMA)-PET volumes with histology compared with mpMRI for the delineation of intraprostatic GTVs, indicating that imaging with molecular targets increases imaging specificity (14). Furthermore, GTVs derived from mpMRI significantly underestimated true tumour volumes compared to PSMA-PET. For intraprostatic radiotherapy boosting, imaging of molecular targets such as PSMA may therefore advantageously replace or be used in addition to conventional mpMRI and provides additional biological characterisation of malignant tissue for dose planning. However, PSMA-PET can intrinsically lead to GTV underestimation due to various technical aspects such as partial volume effects limiting image resolution (15, 16). In addition, PET-based target delineation suffers from the absence of integrated systems such as MRI-LINAC and MRI-US fusion. Conceptually, molecular MRI should provide improved imaging of tumoural features on a biological level over what is to date conventionally afforded by PET imaging. However, despite very extensive research in molecular MRI, especially with nanoparticulate-based contrast agents, clinical translation is yet to be demonstrated. On the other hand, most of the related research has to date focussed on diagnostic applications as opposed to the feasibility of accurately imaging and delineating primary lesions.

Besides the imaging modality itself, a key requirement for molecular MRI is the selection of a biological target specific to the tumour. PSMA is often significantly overexpressed in PCa and as such has become the gold-standard target for molecular imaging of PCa (17). Multiple PSMA ligands are now available for PET imaging with various FDA and EMA-approved PSMA-targeting probes demonstrating success in the clinic. However, loss of PSMA expression has been known to occur in neuroendocrine, androgen receptor-negative PCa, reducing the efficacy of PSMA-targeting probes in these cases. Furthermore, 5-10% of primary PCa or primary PCa lesions are PSMA negative on PET (18, 19). Therefore, imaging of PSMA is not suitable for all patients, warranting the validation of additional imaging targets in PCa (20).

Fibroblast activation protein (FAP) is an extracellular serine protease that is upregulated in stromal components of >90% of epithelial tumours but with low or undetectable expression in normal tissues. In addition, FAP expression correlates with progression and worse prognosis (21, 22). Endothelial cells can also express FAP which contributes to the regulation of tumour angiogenesis, changes in capillary morphology and microvascular reorganization (23). Specifically, FAP has been found to be expressed by tumour endothelial cells during capillary formation but is absent in the mature endothelium (24). Additionally, FAP expression correlates with a significantly increased density of microvessels (25). As such, FAP is potentially a pan-cancer marker and a promising target for molecular imaging and therapy.

125 FAP has been shown to be upregulated in PCa, and is predominantly expressed in cancer
126 associated fibroblasts and reactive stromal cells adjacent to carcinoma cells (26-28). Recent
127 studies demonstrated that in a population of patients with PSMA negative tumours,
128 intermediate to high uptake of a ^{68}Ga-FAP inhibitor was observed in PCa (29, 30).
129 Furthermore, FAP-specific PET imaging of malignancies with low PSMA expression
130 demonstrated more precise results when compared to PSMA-PET (31). Imaging of FAP in PCa
131 has shown promise particularly in castrate resistant prostate cancer (CRPC), with elevated
132 FAP expression also observed in neuroendocrine prostate cancer (NEPC) and patients
133 undergoing neoadjuvant androgen deprivation therapy (ADT) (32).

134 To date, the utility and significance of FAP specific MRI is yet to be assessed. To address this
135 question, here we report on benchmarking the performance of a FAP-targeted iron oxide
136 nanoparticulate MRI agent against PSMA in the delineation of PCa in an orthotopic mouse
137 model. Our experimental approach builds on a previously reported FAP-ligand designed by
138 ligating fragments of existing FAP ligands that were identified by molecular docking studies
139 to contribute most prominently to the specificity and affinity of FAP binding. The FAP and
140 PSMA ligands were substituted from mannose in the FerroTrace maghemite nanoparticulate
141 MRI agent that is presently undergoing clinical trialling as a lymphotropic contrast agent.
142 Using this novel imaging platform, we demonstrate that FAP MRI yields superior tumour
143 contrast and coverage compared to PSMA in a preclinical model of PCa.

144

145 **Materials**

146 The following chemicals were purchased and used as received without further purification.
147 Trifluoroacetic acid, 1-Ethyl-3-(3-dimethylaminopropyl) carbodiimide hydrochloride
148 (EDC.HCl), N-hydroxysuccinimide (NHS), 4-Morpholineethanesulfonic acid, 2-(N-
149 Morpholino)ethanesulfonic acid hydrate (MES hydrate), 10X Phosphate Buffered Saline were
150 purchased from Sigma Aldrich. Acetone and dichloromethane (DCM) we purchased from
151 Chem-Supply. FAP binding ligand was synthesized as previously described (33). PSMA ligand
152 Clu-CO-Lys-$(tBu)_3$ ester (CAS 1025796-31-9) was synthesized by Advanced Molecular
153 Technologies (Scoresby, Victoria, Australia).

154

155 **Analysis of FAP expression in PCa**

156 To evaluate FAP expression in normal prostates and prostate adenocarcinoma, normalized
157 FAP RNAseq (expected count-deseq2+1) data was obtained from the Therapeutically
158 Applicable Research to Generate Effect Treatments initiative (TARGET)/the Cancer Genome
159 Atlas (TCGA)/Genotype Tissue Expression (GTEx) dataset using the UCSC Xena platform
160 (accessed 26/11/2021) (34). Corresponding patient prostate adenocarcinoma pathological T
161 staging was obtained from the TCGA prostate adenocarcinoma (PRAD) data set (accessed
162 26/11/2021). Furthermore, immunohistochemistry staining of FAP in low- and high-grade
163 prostate adenocarcinoma was obtained from the HPA059739 dataset deposited in the Human

164 Protein Atlas (https://www.proteinatlas.org/ENSG00000078098-
165 FAP/pathology/prostate+cancer#) (35).
166
167 **Magnetic nanoparticle synthesis**
168 The core maghemite iron oxide (γ-Fe_2O_3) nanoparticles were synthesised via coprecipitation
169 of iron salts in aqueous solutions and subsequent controlled oxidation using iron nitrate as
170 previously described (36). To achieve *in vivo* stability, the nanoparticles are colloidally
171 stabilised by block copolymers synthesised using reversible addition-fragment chain-transfer
172 (RAFT) polymerisation. The maghemite nanoparticles and RAFT block copolymer coating have
173 been previously developed for the preparation of a lymphotropic MRI agent (FerroTrace,
174 Ferronova) currently undergoing clinical trialling (36). Briefly, two types of block copolymer
175 are attached to the nanoparticle surface: a stabilising-polymer (RAFT-5-MAPC2-15AAM-
176 3PEO) and a targeting polymer with terminal FAP or PSMA ligands (RAFT-5MAPC2-70AAM-
177 PSMA/FAP) in a mole ratio of 70% stabilising to 30% targeting.
178
179 **Preparation of RAFT-5MAPC2-15AAM-3PEO**
180 Polymers were prepared based on a previously published procedure with modifications (37).
181 Methoxy triethylene glycol modified 2-{[butylsulfanyl)cabonothioyl]sulfanyl}propanoic acid
182 (1.0 g), acrylamide (2.8 g), 4,4'-azobis(4-cyanovaleric acid) (0.050 g), dioxane (10 g) and water
183 (10 g) were combined and dissolved before purging with nitrogen gas for 15 minutes and
184 polymerising at 70°C for 2 hours. The mixture was allowed to cool, opened to air, then
185 (methacryloyloxy)-ethyl]phosphonic acid (2.5 g) and 4,4'-azobis(4-cyanovaleric acid) (0.050 g)
186 were added to the reaction mixture. The mixture was purged with nitrogen gas for 15
187 minutes, then heated at 70°C for 4 hours. The polymer was precipitated in acetone, repurified
188 and collected by centrifugation.
189
190 **Preparation of RAFT-5MAPC2-70AAM-PSMA/FAP polymers**
191 RAFT-COOH (2-(((butylthio)carbonothioyl)-thio)-propanoic acid) (0.2 g), 4,4'-azobis(4-
192 cyanovaleric acid) (0.012 g), acrylamide (4.17 g), dioxane (7.8 g) and water (12.1 g) were
193 combined and dissolved. The reaction was magnetically stirred at 70°C for 4 hours in an inert
194 atmosphere. The mixture was allowed to cool, opened to air and [2-(methacryloyloxy)-
195 ethyl]phosphonic acid (0.81 g) and 4,4'-azobis(4-cyanovaleric acid) (0.012 g) were added to
196 the reaction mixture. The reaction was purged with nitrogen gas for 15 minutes before
197 heating to 70°C for 4 hours under magnetic stirring. At this step the RAFT-5MAPC2-70AAM
198 polymer was precipitated in acetone, repurified, collected by centrifugation and stored prior
199 to conjugation with the FAP and PSMA ligands.
200 For preparing RAFT-5MAPC2-70AAM-PSMA, the tert-butyl ester groups of the PSMA ligand
201 [Clu-CO-Lys-$(tBu)_3$ ester] were first removed using 20% trifluoroacetic acid (TFA) in
202 dichloromethane (DCM). Briefly, 20 mg/mL PSMA in 20% TFA in DCM was mixed for 3 hours
203 at room temperature before vacuum drying. The residue was then dissolved in 10-20%

aqueous acetic acid, transferred into a 50 mL falcon tube and a two-fold volume of chloroform was added. The reaction was mixed thoroughly before the layers were allowed to separate and the bottom organic layer containing the protective groups and non-volatile by-products was removed using a needle and syringe. The extraction of the aqueous layer was repeated twice, and it was dried under high vacuum. The residue was dissolved in glacial acetic acid, shell-freezed and lyophilized before use. The NH_2 derivatized FAP ligand was synthesized as previously described and used for the preparation of the RAFT-5MAPC2-70AAM-FAP (31).

PSMA and FAP ligands were conjugated to the RAFT-5MAPC2-70AAM polymer using a carbodiimide coupling reaction. First, 200 mg of poly[[(methacryloyloxy)-ethyl]phosphonic acid]-*block*-poly(acrylamide), EDC.HCl (48 mg) and NHS (12 mg) were dissolved in 10 mL MES buffer (pH 5.0 – 5.5). The solution was mixed in a sonic bath for 10 minutes and the activated polymer was collected by precipitation in acetone followed by centrifugation. Second, FAP/PSMA ligands (12 mg) were dissolved in 100 µL DMSO and diluted to a total volume of 10 mL with 10X PBS buffer prior to addition to the activated polymer. The reaction mixture was stirred for 20 hours. The conjugated polymer was purified using centrifugal filters with a 3 kDa molecular weight cut off membrane. The product was diluted to a final concentration of 50 mg/mL and stored at 4°C until further use.

Preparation of PSMA and FAP nanoparticles

17 mg of RAFT-5MAPC2-15AAM-3PEO and 20 mg of RAFT-5MAPC2-70AAM-PSMA/FAP polymers were dissolved in 2 mL of water and the pH was adjusted to 4 using 0.1M NaOH. The maghemite nanoparticles (45 mg as dried weight) were added to the polymer solution under probe sonication. After mixing for 10 minutes, the pH was adjusted to 5.0 with NaOH (0.1M). Sonication was continued for a total of 30 minutes and the pH was further adjusted stepwise to 6.0 and 7.0. The nanoparticle suspension was purified using a centrifugal filter with a 100 kDa molecular weight cut off membrane. Lastly, the nanoparticles were diluted with 3% saline to obtain a final concentration of 30 mg Fe/mL in 0.9% saline. An illustration of the PSMA/FAP nanoparticle preparation is shown in figure 2a. For the preparation of non-targeted nanoparticles the method described above was repeated except RAFT-5MAPC2-70AAM-PSMA/FAP was replaced by RAFT-5MAPC2-70AAM-COOH.

Nanoparticle characterisation

The morphology of the coated nanoparticles was studied using transmission electron microscope (TEM; JEOL JEM-2100F-HR) equipped with a field emission gun operated at 200 kV. Images were recorded with a CCD Camera (Gatan Orius SC1000). Samples were prepared by placing a small drop of sample suspension in water onto a 200-mesh carbon-coated copper grid (ProSciTech) and subsequently evaporating the water in air.

Dynamic Light Scattering (DLS) data was recorded on a Malvern Instruments Zetasizer Nano ZS at 25°C. The hydrodynamic size of all nanoparticles suspensions was measured at a

243 concentration of 0.1 mg Fe/mL and isotonic saline (0.9%) was used as suspending medium.
244 Measurement duration was chosen as automatic.

245 Surface zeta potential data was acquired using the same instrumentation. The Smoluchowski
246 method was used for the zeta potential measurements. The surface zeta potential of all
247 nanoparticle suspensions was measured at a concentration of 1 mg Fe/mL and 10mM saline
248 was used as the suspending medium.

249

250 **Cancer cell lines and culture conditions**

251 Cells were routinely cultured in RPMI-1640 medium (LNCaP and C32) (Gibco) or Minimum
252 Essential Medium (U87) (Gibco) supplemented with 10% fetal bovine serum (FBS) (Gibco) and
253 1% penicillin/streptomycin (Gibco) in a humidified atmosphere of 5% CO_2 at 37°C. The
254 medium was replaced every 2-3 days and cells were split once they reached 75-80%
255 confluence using TrypLE Express (Gibco). LNCaP and U87 cells were gifted by Professor Lisa
256 Butler and Professor Stuart Pitson, respectively.

257

258 **Flow cytometric analysis of FAP expression in U87 and C32 cells**

259 Cells were harvested from flasks using TrypLE Select (Thermo Fisher), washed in PBS and
260 resuspended in FACS buffer (1% bovine serum albumin (BSA) and 0.04% sodium azide in PBS).
261 Staining for FAP was performed using either a one- or two-step process. For one-step staining,
262 90 µl of cells were incubated with 10 µl of anti-FAP-PE (clone 427819, R&D Systems) for 20
263 minutes at room temperature before washing with FACS buffer. For two-step staining, cells
264 were incubated with mouse anti-FAP (clone 427819, R&D Systems) at a final concentration of
265 5 µg/ml for 20 minutes at room temperature and washed with FACS buffer, then incubated
266 with goat anti-mouse secondary antibody conjugated to AlexaFluor488 (Thermo Fisher #A-
267 11029) at 10 µg/ml for 20 minutes at room temperature, then washed again in FACS buffer.
268 Samples were acquired on an LSR Fortessa or Accuri C6 flow cytometer (both BD Biosciences).
269 Analysis was performed using FCS Express V7 Flow Research Edition (De Novo Software,
270 Pasadena, CA, USA).

271

272 **Magnetic nanoparticle *in vitro* binding assay**

273 To test the binding affinity of the PSMA/FAP nanoparticles, cellular uptake in cells expressing
274 the respective targets was measured *in vitro*. LNCaP cells were seeded in a T25 cell culture
275 flask at a density of 1 x 10^6 cells per flask. C32 cells were seeded in a 6 well plate at a density
276 of 3.5 x 10^5 cells per well in the complete cell culture medium as described above. The cells
277 were placed in a 37°C, 5% CO_2 incubator and allowed to adhere for 24 hours. PSMA, FAP and
278 control unconjugated nanoparticle suspensions were prepared at a concentration of 0.150
279 mg Fe/mL in cell culture medium. 6 mL of PSMA or control nanoparticle suspension was added
280 to each flask containing adherent LNCaP cells or 1 mL of FAP and control nanoparticle
281 suspension was added to each well containing adherent C32 cells. Three replicates were used
282 to test each of the nanoparticle formulations. Cells were incubated with the nanoparticle

283 suspensions for 24 hours in an incubator at 37°C in 5% CO_2 humidified atmosphere. After
284 incubation, cells were washed 3 times with PBS, detached using TrypLE Express and cell
285 pellets were collected via centrifugation at 500 g for 5 minutes. The cell pellets were washed
286 twice with PBS and were dried at 60°C overnight using a heating block. The dried cell pellets
287 were digested with trace metal grade nitric and hydrochloric acid (1:1 ratio by volume).
288 Digested samples were diluted with water to a total volume of 10 mL or 3 mL for LNCaP PSMA
289 nanoparticles and C32 FAP nanoparticle samples, respectively. Iron concentration was
290 measured by inductively coupled plasma mass spectroscopy (ICP-MS).
291

292 **Preclinical study in an orthotopic prostate cancer murine model**

293 All animal experiments were approved by the Animal Ethics Committee of the South
294 Australian Health and Medical Research Institute (SAHMRI) and were conducted in
295 accordance with Australian National Health and Medical Research Council (NHMRC)
296 guidelines and the Animal Welfare Act and conformed to the Australian Code for the Care and
297 Use of Animals for Scientific Purposes. Male NOD scid gamma (NSG) aged 6-8 weeks were
298 bred and group-housed in a specific pathogen free environment at the SAHMRI. Animals had
299 *ad libitum* access to food and water and were clinically assessed daily. Mice were humanely
300 euthanized via CO_2 inhalation to remove tissues.

301 Intraprostatic injection of cancer cells was performed as previously described (38). Briefly, a
302 lower midline incision was made, the bladder and prostate were externalised and 10 µL of
303 RPMI-1640 containing 1 x 10^6 LNCaP cells were injected into the anterior prostate using a
304 precooled Hamilton syringe. To analyse tumour engraftment and growth, mice underwent
305 weekly *in vivo* bioluminescence imaging (IVIS, Perkin Elmer), approximately 15-20 minutes
306 post intraperitoneal injection with 150 mg/kg D-luciferin potassium salt.
307

308 **Magnetic Resonance Imaging**

309 After 5-6 weeks of tumour growth, mice were intravenously injected with 40 mg Fe/kg
310 nanoparticles in up to 100 µL of saline. Healthy mice with no tumours were used as controls.
311 After a 24-hour period, mice were anaesthetised with 2% isoflurane in oxygen and were
312 intraperitoneally injected with an overdose of pentobarbital prior to transcardial perfusion
313 with 4% paraformaldehyde. Mice were postfixed in 4% paraformaldehyde prior to storage in
314 PBS with 0.1% sodium azide. Mice underwent *ex vivo* T2-weighted multiple graded echo
315 sequence acquired using a 16.4T Bruker Avance scanner (Bruker BioSpin, GmbH), with a 30
316 mm SAW coil (M2M Imaging, Brisbane, Australia) (repetition time 40 ms, echo time 10 ms,
317 number of averages 1, slice thickness 0.1 mm) or fast low angle shot (FLASH) sequence using
318 9.4T Bruker BioSpec scanner (Bruker BioSpin, GmbH, repetition time 50 ms, echo time 10 ms,
319 number of averages 1, slice thickness 0.1 mm). At the completion of scans, tumours were
320 excised and underwent FLASH scans using a 11.7T Bruker Avance II scanner (Bruker BioSpin,
321 GmbH, repetition time 100 ms, echo time 5.34 ms, number of averages 10, slice thickness 0.2

322 mm). All imaging was performed at room temperature. Horos was used to view scans
323 (Horosproject.org, sponsored by Nimble Co LLC d/b/a Purview in Annapolis, MD USA).

324 Calculations of proportions of black pixels were based on protocols previously reported (39,
325 40). In brief, three regions of interest (ROI) were manually drawn over the prostate tumours
326 in whole body MR scans using ImageJ software (Bethesda, Maryland, USA) (41). Pixel intensity
327 histograms were generated for each ROI. A low intensity pixel threshold value was set, based
328 on the visual analysis of threshold peaks.

329 Tumour T2 maps were generated from 16.4T and 9.4T T2-weighted MR images using an in-
330 house code written in MATLAB (version 9.12.0 (R022a), The MathWorks, Inc., Natick,
331 Massachusetts, United States). R2 values were calculated from T2 maps using a mono-
332 exponential proton transverse relaxation method as previously published, using in-house
333 code written in MATLAB(42). In agreement with previously published studies, we found
334 negligible differences in R2 values between the two fields strengths (43, 44) and as such they
335 have been combined in the results. T2 map tumour border ROIs were manually drawn
336 throughout all tumour slices by an experienced MRI technician and the R2 distribution was
337 calculated for each tumour. The resulting R2 histograms were plotted and the resulting
338 Gaussian curves were used to calculate the change in mean R2 and differences in area under
339 the curve.

340

341 **Haematoxylin and Eosin and Prussian Blue Staining**

342 After *ex vivo* MR imaging, excised tumours, spleens, kidneys and livers were mounted in
343 paraffin and 4 µm thick sections were stained with hematoxylin and eosin (H&E) or Prussian
344 blue using standard protocols. Briefly, for Prussian blue staining sections were brought to
345 distilled water and stained in an equal part mixture of potassium ferrocyanide and
346 hydrochloric acid for 10 minutes, prior to washing in distilled water and counterstain with
347 neutral red stain. For H&E staining, slides were stained using Dako automated slide stainer
348 (Agilent, United States). Briefly, slides were brought to distilled water prior to staining with
349 haematoxylin for 1 minute, bluing for 1 minute and eosin staining for 4.5 minutes. Images
350 were processed using a Nanozoomer (Hamamatsu, Japan) and were visualized using ImageJ
351 software (Bethesda, Maryland, United States). The percentage area of positive/blue Prussian
352 Blue staining was calculated by setting colour thresholds using ImageJ software.

353

354 **Tissue Immunohistochemistry**

355 4 µm paraffin embedded tumour serial sections were used to compare Prussian blue staining
356 with CD31, PSMA and FAP immunohistochemistry. Staining was performed using rabbit
357 specific HRP/DAB detection kit (Abcam) following the manufacturer's instructions, with
358 modifications. Briefly, after hydration through a series of ethanol, sections were treated with
359 hydrogen peroxide blocking for 10 minutes. Antigen retrieval was performed using pH 6 10
360 mM citrate buffer at 98°C for 30 minutes and then incubated with 10% normal goat serum
361 for 1 hour for protein blocking. The sections were incubated overnight at 4°C with anti-CD31

antibody (1:500, Abcam ab182981, EPR17259) or anti-FAP antibody (1:300, Abcam ab28244) or anti-PSMA antibody (1:500, Abcam ab76104, EP3253). After washing, sections were treated with biotinylated antibody and streptavidin peroxidase and developed with 3,3'-Diaminobenzidine (DAB) (all provided in kit). Images were processed using a Nanozoomer (Hamamatsu, Japan) and were visualized using ImageJ software (Bethesda, Maryland, USA).

The percentage area of positive staining was calculated by setting colour thresholds using ImageJ. Entire images have been adjusted for brightness, contrast and exposure, consistently between stains.

Statistical analyses

Data are expressed as mean ± SEM in all cases. The significance of results were determined by unpaired t testing or one way ANOVA. Differences with a p value of less than 0.05 were considered to be statistically significant. The relationship between FAP expression and PSA levels and Gleason scores were assessed using simple linear regression. The relationship between the area of positive Prussian blue staining and CD31, FAP and PSMA staining were assessed using Spearman rank correlations using Graphpad software.

Results

Human FAP expression in the normal prostate and prostate adenocarcinoma

Analysis of available transcriptomic data showed a significant increase in FAP expression from normal prostate to adenocarcinoma ($p<0.0001$) (figure 1a). Further analysis comparing the expression between pathological T stages demonstrated significant increases from normal prostate to early stage (I and II) ($p<0.0001$) and to locally advanced (stage III) ($p<0.0001$). However, there was no additional significant increase to advanced (IV) ($p>0.05$) (figure 1b). FAP expression was further demonstrated by FAP immunohistochemistry in biopsies of low- and high-grade prostate adenocarcinoma (figures 1e and f). Linear correlation of Gleason score with FAP expression showed a weak positive relationship ($R^2 = 0.072$) (figure 1d), whereas there was no correlation demonstrated with PSA ($R^2 = 0.005$) (figure 1c).

Characterization of magnetic nanoparticles

To assess the characteristics of the prepared PSMA and FAP nanoparticles, a set of physico-chemical characterisations were carried out. TEM images (figure 2b and c), taken at 60K x magnification, showed near spherical, evenly dispersed FAP and PSMA nanoparticles even when dried on a carbon film. DLS measurements of the hydrodynamic diameters confirmed that all of the coated nanoparticles have a narrow size distribution with an average hydrodynamic size of 60–65 nm when measured in physiological saline (figure 2d). All nanoparticles were also characterised with similar surface charge ranging from an average of -17 mV to -20 mV (figure 2e).

In vitro binding studies

401 The binding affinities of the prepared PSMA/FAP nanoparticles to the PSMA and FAP
402 receptors were evaluated *in vitro* by comparing their cellular uptake in cancer cell lines which
403 overexpress the receptors of interest. For nanoparticles used in biomedical applications, it is
404 important to take into consideration the potential protein adsorption onto the nanoparticle's
405 surface which can impact the binding activity, also known as the protein corona (45, 46). For
406 taking the formation of the protein corona into account, cellular uptake studies were
407 performed in full cell culture media containing 10% serum and incubation time was prolonged
408 to a 24-hour period.

409 First, the binding activity of PSMA nanoparticles was tested in the PSMA expressing cell line
410 LNCaP (47). The results presented in figure 2h indicated that the non-targeted nanoparticles
411 had a much lower cellular uptake compared to the targeted PSMA nanoparticles. Similarly,
412 the binding activity of FAP nanoparticles was tested in the human melanoma cell line C32 as
413 the FAP receptor is expressed in melanoma cell lines (48). Flow cytometric analysis of FAP
414 expression demonstrated that C32 cells had approximately 25% greater proportion of FAP-
415 positive cells in contrast to U87 cells, which had been previously demonstrated to have high
416 levels of FAP expression (figure 2f). The targeted FAP nanoparticles had an uptake almost
417 twice as high as the non-targeted nanoparticles (figure 2g). Considering the similar
418 physicochemical features of the PSMA/FAP nanoparticles when compared with the
419 unconjugated control nanoparticles, these cellular uptake data validate the chemical design
420 and specific binding affinity of the conjugated nanoparticles to their respective targets.

421

422 **Magnetic resonance imaging of orthotopic prostate tumours**

423 There was a significant increase in tumour contrast enhancement on T_2-W whole body MRI
424 after administration of both PSMA nanoparticles and FAP nanoparticles in mice bearing
425 orthotopic LNCaP tumours compared to the unconjugated control nanoparticle group, as
426 quantitatively demonstrated by the proportions of intratumoural black pixels (figure 3,
427 $p=0.0358$ for PSMA nanoparticles and $p<0.0001$ for FAP nanoparticles, n=3-4 per group). FAP
428 nanoparticle administration yielded ~15% improvement of tumour contrast enhancement
429 compared to PSMA nanoparticles ($p=0.0004$, n=4 per group). Administration of non-targeted
430 control nanoparticles resulted in a modest, nonsignificant increase in tumour contrast relative
431 to the no nanoparticle control group ($p=0.2615$, n=3 per group).

432 To better assess the potential for tumour delineation, changes in R2 distribution between
433 prostate tumours and healthy prostates were examined. Specifically, tumour borders were
434 compared against the healthy prostate in animals administered the same particles. Due to
435 the overgrowth of LNCaP tumours in the prostate, these calculations were performed using
436 separate animals. PSMA and FAP nanoparticles induced a shift in contrast in tumours (figure
437 4a and b), relative to control prostates, respectively. The percentage change in mean R2
438 relative to the healthy control with the same particles was greater in FAP nanoparticles (mean
439 change 107%) than PSMA nanoparticles (mean change 70.14%) (figure 4c, $p<0.05$). More
440 specifically, FAP nanoparticles had a greater percentage difference of area under the curve
441 relative to the healthy control prostate in contrast to PSMA nanoparticles (figure 4d,

442 p<0.001). Pixels in this area under the curve which is not covered by the control may
443 contribute towards the change in contrast required for tumour delineation within the healthy
444 prostate.
445
446 **Distribution of magnetic nanoparticles in tissues**
447 To examine the intratumoural distribution of non-heme iron after the administration of the
448 PSMA/FAP nanoparticles, Prussian blue staining was performed on sections of LNCaP
449 orthotopic prostate tumours and normal prostates (figure 5a). No positive staining was
450 observed in normal prostate sections. The absence of Prussian blue staining in sections of
451 normal prostate for mice administrated with control, FAP and PSMA nanoparticles confirmed
452 the lack of significant nanoparticle accumulation in the absence of orthotopic tumours. LNCaP
453 tumours also showed minimal positive basal staining. In agreement with the MRI data,
454 modest Prussian blue staining was observed after administration of control nanoparticles. On
455 the other hand, LNCaP tumours showed significant positive staining after the administration
456 of PSMA and FAP nanoparticles, of which the staining was concentrated on the tumour
457 periphery. Both PSMA and FAP nanoparticles demonstrated heterogenous intermittent
458 intratumoural staining, some of which was suggestive of blood vessel staining, of which the
459 frequency was greater in FAP nanoparticles compared to PSMA nanoparticles.
460 To better understand the distribution of the nanoparticles within tumours, positive Prussian
461 blue stained areas were correlated with positive areas for CD31 or PSMA or FAP (figures 5b-
462 e and representative images figures 5f-h and 5j-l). It was found that Prussian blue staining as
463 a result of FAP nanoparticles correlated more strongly with positive area of CD31 staining
464 compared to PSMA targeted particles (figures 5b and d). Furthermore, FAP nanoparticles had
465 a stronger correlation with Prussian blue staining and positive staining of FAP, when
466 compared with PSMA particles Prussian blue staining and PSMA expression (figures 5c and e).
467 These relationships may be explained by the tumoural distribution of FAP and PSMA
468 expression, as PSMA is expressed by LNCaP cells and therefore throughout the tumours, in
469 contrast to FAP, which is primarily expressed by stromal components including perivascular
470 regions. To confirm the distribution of the iron oxide nanoparticles and their effect on MRI,
471 high resolution MR imaging of resected tumours treated with either FAP nanoparticles or
472 PSMA nanoparticles was performed. Preferential contrast enhancement was observed at the
473 tumour peripheries, in contrast to homogenous contrast enhancement throughout the
474 tumours (figures 5i and m), suggesting preferential accumulation of the nanoparticles to the
475 highly vascularised tumour periphery, in qualitative agreement with the Prussian blue
476 staining data.
477 Finally, Prussian blue staining was performed to assess the distribution of iron oxide
478 nanoparticles in the kidney, liver and spleen in orthotopic tumour mice (figure 6). Through
479 visual assessment there was no increase in Prussian blue staining in the spleen and kidneys in
480 all nanoparticle groups when compared to the no particle control. As expected, we observed
481 a marginal increase in Prussian blue staining in the liver compared to the no nanoparticle
482 control, which was consistent among all nanoparticles. Furthermore, to preliminarily assess

483 potential acute toxicities, H&E staining was performed on the kidneys, liver and spleen of
484 LNCaP tumour bearing mice (figure 6). No changes in tissue morphology were observed across
485 the kidneys, liver and spleen in a control, PSMA and FAP-targeting nanoparticles, when
486 compared to the no nanoparticle control.
487
488 **Discussion**
489 Focal boost therapies of PCa aim to selectively eliminate dominant intraprostatic malignant
490 lesions whilst sparing surrounding off-target tissues, and in doing so achieving oncological
491 outcomes similar to those afforded by whole gland treatment but with reduced adverse
492 effects. To enable effective focal treatment with contemporary treatment approaches
493 including image guided RT, target volumes and safety margins must be precisely defined.
494 Current MRI techniques such as mpMRI have yielded promising performance in providing
495 treatment guidance but are susceptible to underestimation of the true tumour volume (49)
496 and are time and resource demanding. This may be improved through the utilisation of
497 molecular MRI targeting tumour markers.
498 Targeting of pan-cancer marker FAP has practise-redefining potential in the treatment of solid
499 tumours such as PCa, through improved boundary delineation, possibly enabling the use of
500 focal lesion ablative microboosts. FAP is predominantly expressed on cancer associated
501 fibroblasts (CAFs) which reside in the tumour stroma and expression is present in virtually all
502 solid tumours. In addition, unlike cancer cells, CAFs are not undergoing constant mutation,
503 adding to the promising targeting qualities of FAP (33, 50, 51). Prostate tumours can have
504 over 50% stromal component, which can be greater in cases of desmoplastic reaction (29). As
505 such, targeting of the tumour stroma may provide increased imaging sensitivity and contrast
506 agent retention at the intraprostatic target site compared with targeting of the tumour cells
507 themselves. PCa metastases have also been demonstrated to be FAP positive, possibly
508 enabling focal metastatic lesion ablative treatment, with further investigation required. In
509 support of this train of thought, pilot studies using PSMA-PET have shown efficacy in image-
510 guided radiotherapy of metastases for the treatment of oligorecurrent PCa (52). In another
511 study, 1.5T MRI guided stereotactic body RT by LINAC guided by PSMA-PET produced
512 encouraging oncological and tolerability results in the management of oligometastatic
513 castration sensitive prostate cancer (53). Recently, FAP-targeted PET has demonstrated fair
514 to good interobserver agreement rates in the detection of organ and lymph node metastases
515 across a variety of tumour types (54). There are yet to be clinical studies investigating the use
516 of molecular MRI contrast agents in image-guided RT. FAP-targeted MRI-guided radiotherapy
517 may also prove beneficial in palliative radiotherapy, particularly in reducing pain arising from
518 PCa bone metastases, leading to improved quality of life (55).
519 FAP-specific imaging may be most beneficial in late stage and clinically aggressive cancers, in
520 which FAP expression can be more pronounced than PSMA and in cases with doubtful lesions,
521 therapy failure and/or PSMA downregulation or negative disease (31, 56). Patients
522 undergoing long-term ADT may have a decreased detection sensitivity on PSMA imaging due
523 to downregulation of the receptor, although this issue may be mitigated by ceasing ADT prior

524 to imaging studies (57). Current literature suggests that short-term ADT upregulates PSMA,
525 suggesting that PSMA-targeted imaging is suitable in these patients.

526 Although various FAP and PSMA-specific PET tracers are being actively developed, PET
527 imaging lacks the resolution that is optimal for focal radiotherapy. MR boasts superior soft
528 tissue contrast, visualization of organ movement and the ability to monitor changes in tumour
529 and tissue physiology, enabling improved adaptation of target volumes between RT
530 treatment fractions (58). However, interpretation of PCa mpMRI is susceptible to significant
531 interpretation variability as demonstrated by discordance in prostate imaging reporting and
532 data system (PIRADS) score assignment and cancer yield by radiologists (59). MRI provides
533 high resolution 3D morphological information which can be enhanced with the use of
534 magnetic core nanoparticles which cause hypointense signals (darkening) on MR imaging by
535 decreasing the relaxation times of protons in surrounding water molecules. This exogenous
536 contrast of the tumour may lead to decreased inter-observer variability of GTV delineation.
537 The utilisation of FAP or PSMA-targeted MRI may also improve the delineation of low-grade
538 disease, such as Gleason 3+3 cancers which are often missed on MRI (60). Furthermore, it
539 was found that T2-weighted MRI underestimated GTVs, longest axis and pathological tumour
540 extent in nearly every case. Furthermore, cellular composition, density and interstitial stromal
541 space have an effect on diffusion-weighted imaging (DWI) and derived apparent diffusion
542 coefficient (ADC) maps, which may contribute towards the underestimation of GTVs (61).

543 In this study we designed, synthesized and characterized FAP and PSMA targeted iron oxide
544 nanoparticles for molecular MRI and comparatively assessed imaging performance *in vivo* in
545 an orthotopic model of prostate cancer. To our knowledge, this is the first report describing
546 the use of FAP specific MRI. The ligand targeted nanoparticles are modified from a
547 lymphotropic agent that has been validated in a large animal model and presently undergoing
548 clinical trial (ACTRN12620000831987). This design relies on targeting and stabilising block
549 copolymers of different lengths that enable efficient targeting using small molecule ligands
550 as shown in the excellent binding affinity observed here *in vitro* with PSMA and FAP
551 expressing cells.

552 Both FAP and PSMA targeted nanoparticles yielded improved tumour accumulation as shown
553 by increase in MRI contrast in orthotopic tumour bearing mice compared to non-targeted
554 nanoparticles. It is noteworthy that FAP-targeted MRI outperformed MRI targeting PSMA, the
555 current clinical imaging benchmark, in contrast enhancement and delineation of prostate
556 tumours in the orthotopic mouse model used here. The LNCaP tumour model was selected
557 for this study as it commonly used for preclinical studies of PSMA specific diagnostic and
558 therapeutic agents. Additionally, the expression of FAP in the stroma of orthotopic LNCaP
559 tumours has been previously demonstrated as indicated by colocalization of both FAP and a-
560 smooth muscle actin (62). The excellent imaging performance of the FAP nanoparticles
561 observed here could be explained by the distribution of FAP expression, which predominantly
562 occurs in the stroma and vasculature, and might therefore be more accessible to
563 nanoparticulate imaging agents than markers expressed by tumour cells. Not surprisingly, the
564 enhanced contrast associated to the presence of the iron oxide nanoparticles was found to

be more pronounced at the periphery of the orthotopic tumours. This can be explained by the higher density of vascular structures at the periphery of such orthotopic models (63). As expected, unconjugated nanoparticles provided a modest improvement in the MRI contrast. Non-specific accumulation of nanoparticles within solid tumours is typically observed in preclinical mouse models, although the precise mechanisms are still controversial (64). Enhanced tumour contrast on MRI has also been confirmed in several clinical trials for various dextran-coated iron oxide nanoparticles (65). The ongoing NCT04682847 trial investigates the use of Ferumoxytol, a non-targeted iron oxide nanoparticle, in MRI-LINAC treatment of hepatic cancer.

Considering the pan-cancer nature of FAP expression in the stroma of solid tumours, FAP-specific MRI with rationally designed iron oxide nanoparticles may prove useful in the delineation of other solid tumours such as gastrointestinal and brain cancer. In the future, FAP specific MRI may also be useful to guide RT with proton therapies, thereby fully harnessing the uniquely precise dose deposition afforded by this technique (66).

Disclosures

ND, VM, RM, MN, PL and BT hold patents for FAP imaging technologies. BT is a founding member and shareholder of Ferronova Pty Ltd. ND and VM salaries are funded through Australian National Health and Medical Research Council grant 1158-755 and each undertake duties involving research and development that contribute to Ferronova Pty Ltd. AS and MN are employees of Ferronova Pty Ltd.

Funding

This research was supported by funding from an Australian National Health and Medical Research Council grant number 1158-755 (BT as chief investigator A).

Acknowledgements

We acknowledge the facilities and scientific and technical assistance of the National Imaging Facility, a National Collaborative Research Infrastructure Strategy (NCRIS) capability, at SAHMRI PIRL, the University of Western Sydney and the University of Queensland.

CRediT author statement

Nicole Dmochowska: conceptualization, methodology, validation, formal analysis, investigation, resources, data curation, writing – original draft, writing – review & editing, visualization, project administration. **Valentina Milanova:** conceptualization, methodology, validation, formal analysis, investigation, resources, data curation, writing – original draft, writing – review & editing. **Ramesh Mukkamala:** resources, writing – review & editing. **Kwok Keung Chow:** methodology, validation, formal analysis, data curation, writing – review & editing. **Nguyen T. H. Pham:** methodology, validation, investigation, resources, data curation. **Madduri Srinivasarao:** resources, writing – review & editing. **Lisa Ebert:** methodology,

validation, formal analysis, investigation, data curation, writing – review & editing. **Timothy Stait-Gardner:** resources, data curation, writing – review & editing. **Hien Le:** writing – review & editing. **Anil Shetty:** methodology, writing – review & editing. **Melanie Nelson:** methodology, writing – review & editing. **Phil Low:** resources, writing – review & editing, funding acquisition. **Benjamin Thierry:** conceptualization, methodology, resources, writing – original draft, writing – review & editing, visualization, supervision, project administration, funding acquisition.

References

1.Sung H, Ferlay J, Siegel RL, Laversanne M, Soerjomataram I, Jemal A, et al. Global Cancer Statistics 2020: GLOBOCAN Estimates of Incidence and Mortality Worldwide for 36 Cancers in 185 Countries. *CA Cancer J Clin* 2021;**71**:209-49.

2.Goodman CD, Fakir H, Pautler S, Chin J, Bauman GS. Dosimetric Evaluation of PSMA PET-Delineated Dominant Intraprostatic Lesion Simultaneous Infield Boosts. *Adv Radiat Oncol* 2020;**5**:212-20.

3.Viani GA, Stefano EJ, Afonso SL. Higher-than-conventional radiation doses in localized prostate cancer treatment: a meta-analysis of randomized, controlled trials. *Int J Radiat Oncol Biol Phys* 2009;**74**:1405-18.

4.Mazariego CG, Egger S, King MT, Juraskova I, Woo H, Berry M, et al. Fifteen year quality of life outcomes in men with localised prostate cancer: population based Australian prospective study. *BMJ* 2020;**371**:m3503.

5.Matta R, Chapple CR, Fisch M, Heidenreich A, Herschorn S, Kodama RT, et al. Pelvic Complications After Prostate Cancer Radiation Therapy and Their Management: An International Collaborative Narrative Review. *Eur Urol* 2019;**75**:464-76.

6.Arrayeh E, Westphalen AC, Kurhanewicz J, Roach M, 3rd, Jung AJ, Carroll PR, et al. Does local recurrence of prostate cancer after radiation therapy occur at the site of primary tumor? Results of a longitudinal MRI and MRSI study. *Int J Radiat Oncol Biol Phys* 2012;**82**:e787-93.

7.Pucar D, Hricak H, Shukla-Dave A, Kuroiwa K, Drobnjak M, Eastham J, et al. Clinically significant prostate cancer local recurrence after radiation therapy occurs at the site of primary tumor: magnetic resonance imaging and step-section pathology evidence. *Int J Radiat Oncol Biol Phys* 2007;**69**:62-9.

8.Murray JR, Tree AC, Alexander EJ, Sohaib A, Hazell S, Thomas K, et al. Standard and Hypofractionated Dose Escalation to Intraprostatic Tumor Nodules in Localized Prostate Cancer: Efficacy and Toxicity in the DELINEATE Trial. *Int J Radiat Oncol Biol Phys* 2020;**106**:715-24.

9.Kerkmeijer LGW, Groen VH, Pos FJ, Haustermans K, Monninkhof EM, Smeenk RJ, et al. Focal Boost to the Intraprostatic Tumor in External Beam Radiotherapy for Patients With Localized Prostate Cancer: Results From the FLAME Randomized Phase III Trial. *J Clin Oncol* 2021;**39**:787-96.

10.Ghai S, Finelli A, Corr K, Chan R, Jokhu S, Li X, et al. MRI-guided Focused Ultrasound Ablation for Localized Intermediate-Risk Prostate Cancer: Early Results of a Phase II Trial. *Radiology* 2021;**298**:695-703.

683 11.Walser E, Nance A, Ynalvez L, Yong S, Aoughsten JS, Eyzaguirre EJ, et al. Focal Laser Ablation
684 of Prostate Cancer: Results in 120 Patients with Low- to Intermediate-Risk Disease. *J Vasc*
685 *Interv Radiol* 2019;**30**:401-9 e2.

686 12.Muller BG, Shih JH, Sankineni S, Marko J, Rais-Bahrami S, George AK, et al. Prostate Cancer:
687 Interobserver Agreement and Accuracy with the Revised Prostate Imaging Reporting and Data
688 System at Multiparametric MR Imaging. *Radiology* 2015;**277**:741-50.

689 13.Ahmed HU, El-Shater Bosaily A, Brown LC, Gabe R, Kaplan R, Parmar MK, et al. Diagnostic
690 accuracy of multi-parametric MRI and TRUS biopsy in prostate cancer (PROMIS): a paired
691 validating confirmatory study. *Lancet* 2017;**389**:815-22.

692 14.Bettermann AS, Zamboglou C, Kiefer S, Jilg CA, Spohn S, Kranz-Rudolph J, et al. [(68)Ga-
693]PSMA-11 PET/CT and multiparametric MRI for gross tumor volume delineation in a slice by
694 slice analysis with whole mount histopathology as a reference standard - Implications for focal
695 radiotherapy planning in primary prostate cancer. *Radiother Oncol* 2019;**141**:214-9.

696 15.Piert M, Shankar PR, Montgomery J, Kunju LP, Rogers V, Siddiqui J, et al. Accuracy of tumor
697 segmentation from multi-parametric prostate MRI and (18)F-choline PET/CT for focal
698 prostate cancer therapy applications. *EJNMMI Res* 2018;**8**:23.

699 16.Piert M, Park H, Khan A, Siddiqui J, Hussain H, Chenevert T, et al. Detection of aggressive
700 primary prostate cancer with 11C-choline PET/CT using multimodality fusion techniques. *J*
701 *Nucl Med* 2009;**50**:1585-93.

702 17.Bouchelouche K, Choyke PL, Capala J. Prostate specific membrane antigen- a target for
703 imaging and therapy with radionuclides. *Discov Med* 2010;**9**:55-61.

704 18.Budaus L, Leyh-Bannurah SR, Salomon G, Michl U, Heinzer H, Huland H, et al. Initial
705 Experience of (68)Ga-PSMA PET/CT Imaging in High-risk Prostate Cancer Patients Prior to
706 Radical Prostatectomy. *Eur Urol* 2016;**69**:393-6.

707 19.Maurer T, Gschwend JE, Rauscher I, Souvatzoglou M, Haller B, Weirich G, et al. Diagnostic
708 Efficacy of (68)Gallium-PSMA Positron Emission Tomography Compared to Conventional
709 Imaging for Lymph Node Staging of 130 Consecutive Patients with Intermediate to High Risk
710 Prostate Cancer. *J Urol* 2016;**195**:1436-43.

711 20.Tosoian JJ, Gorin MA, Rowe SP, Andreas D, Szabo Z, Pienta KJ, et al. Correlation of PSMA-
712 Targeted (18)F-DCFPyL PET/CT Findings With Immunohistochemical and Genomic Data in a
713 Patient With Metastatic Neuroendocrine Prostate Cancer. *Clin Genitourin Cancer*
714 2017;**15**:e65-e8.

715 21.Zi F, He J, He D, Li Y, Yang L, Cai Z. Fibroblast activation protein alpha in tumor
716 microenvironment: recent progression and implications (review). *Mol Med Rep*
717 2015;**11**:3203-11.

718 22.Liu F, Qi L, Liu B, Liu J, Zhang H, Che D, et al. Fibroblast activation protein overexpression
719 and clinical implications in solid tumors: a meta-analysis. *PLoS One* 2015;**10**:e0116683.

720 23.Aimes RT, Zijlstra A, Hooper JD, Ogbourne SM, Sit ML, Fuchs S, et al. Endothelial cell serine
721 proteases expressed during vascular morphogenesis and angiogenesis. *Thromb Haemost*
722 2003;**89**:561-72.

723 24.Xin L, Gao J, Zheng Z, Chen Y, Lv S, Zhao Z, et al. Fibroblast Activation Protein-α as a Target
724 in the Bench-to-Bedside Diagnosis and Treatment of Tumors: A Narrative Review. *Frontiers in*
725 *Oncology* 2021;**11**.

726 25.Gao LM, Wang F, Zheng Y, Fu ZZ, Zheng L, Chen LL. Roles of Fibroblast Activation Protein
727 and Hepatocyte Growth Factor Expressions in Angiogenesis and Metastasis of Gastric Cancer.
728 *Pathol Oncol Res* 2019;**25**:369-76.

729 26.Giannoni E, Bianchini F, Masieri L, Serni S, Torre E, Calorini L, et al. Reciprocal activation of
730 prostate cancer cells and cancer-associated fibroblasts stimulates epithelial-mesenchymal
731 transition and cancer stemness. *Cancer Res* 2010;**70**:6945-56.

732 27.LeBeau AM, Brennen WN, Aggarwal S, Denmeade SR. Targeting the cancer stroma with a
733 fibroblast activation protein-activated promelittin protoxin. *Mol Cancer Ther* 2009;**8**:1378-86.

734 28.Tuxhorn JA, Ayala GE, Smith MJ, Smith VC, Dang TD, Rowley DR. Reactive stroma in human
735 prostate cancer: induction of myofibroblast phenotype and extracellular matrix remodeling.
736 *Clin Cancer Res* 2002;**8**:2912-23.

737 29.Hintz HM, Gallant JP, Vander Griend DJ, Coleman IM, Nelson PS, LeBeau AM. Imaging
738 Fibroblast Activation Protein Alpha Improves Diagnosis of Metastatic Prostate Cancer with
739 Positron Emission Tomography. *Clin Cancer Res* 2020;**26**:4882-91.

740 30.Khreish F, Rosar F, Kratochwil C, Giesel FL, Haberkorn U, Ezziddin S. Positive FAPI-PET/CT
741 in a metastatic castration-resistant prostate cancer patient with PSMA-negative/FDG-positive
742 disease. *Eur J Nucl Med Mol Imaging* 2020;**47**:2040-1.

743 31.Kessel K, Seifert R, Weckesser M, Boegemann M, Huss S, Kratochwil C, et al. Prostate-
744 specific membrane antigen and fibroblast activation protein distribution in prostate cancer:
745 preliminary data on immunohistochemistry and PET imaging. *Ann Nucl Med* 2022;**36**:293-301.

746 32.Kesch C, Yirga L, Dendl K, Handke A, Darr C, Krafft U, et al. High fibroblast-activation-
747 protein expression in castration-resistant prostate cancer supports the use of FAPI-molecular
748 theranostics. *Eur J Nucl Med Mol Imaging* 2021;**49**:385-9.

749 33.Roy J, Hettiarachchi SU, Kaake M, Mukkamala R, Low PS. Design and validation of fibroblast
750 activation protein alpha targeted imaging and therapeutic agents. *Theranostics*
751 2020;**10**:5778-89.

752 34.Goldman MJ, Craft B, Hastie M, Repecka K, McDade F, Kamath A, et al. Visualizing and
753 interpreting cancer genomics data via the Xena platform. *Nat Biotechnol* 2020;**38**:675-8.

754 35.Uhlen M, Fagerberg L, Hallstrom BM, Lindskog C, Oksvold P, Mardinoglu A, et al.
755 Proteomics. Tissue-based map of the human proteome. *Science* 2015;**347**:1260419.

756 36.Krishnan G, Cousins A, Pham N, Milanova V, Nelson M, Krishnan S, et al. Preclinical
757 evaluation of a mannose-labeled magnetic tracer for enhanced sentinel lymph node retention
758 in the head and neck. *Nanomedicine* 2022:102546.

759 37.Bryce NS, Pham BTT, Fong NWS, Jain N, Pan EH, Whan RM, et al. The composition and end-
760 group functionality of sterically stabilized nanoparticles enhances the effectiveness of co-
761 administered cytotoxins. *Biomater Sci* 2013;**1**:1260-72.

762 38.Linxweiler J, Korbel C, Muller A, Hammer M, Veith C, Bohle RM, et al. A novel mouse model
763 of human prostate cancer to study intraprostatic tumor growth and the development of
764 lymph node metastases. *Prostate* 2018;**78**:664-75.

765 39.Ngen EJ, Benham Azad B, Boinapally S, Lisok A, Brummet M, Jacob D, et al. MRI Assessment
766 of Prostate-Specific Membrane Antigen (PSMA) Targeting by a PSMA-Targeted Magnetic
767 Nanoparticle: Potential for Image-Guided Therapy. *Mol Pharm* 2019;**16**:2060-8.

768 40.Ngen EJ, Chen Y, Azad BB, Boinapally S, Jacob D, Lisok A, et al. Prostate-specific membrane
769 antigen (PSMA)-targeted photodynamic therapy enhances the delivery of PSMA-targeted
770 magnetic nanoparticles to PSMA-expressing prostate tumors. *Nanotheranostics* 2021;**5**:182-
771 96.

772 41.Schneider CA, Rasband WS, Eliceiri KW. NIH Image to ImageJ: 25 years of image analysis.
773 *Nat Methods* 2012;**9**:671-5.

774 42.Clark PR, Chua-anusorn W, St Pierre TG. Bi-exponential proton transverse relaxation rate
775 (R2) image analysis using RF field intensity-weighted spin density projection: potential for R2
776 measurement of iron-loaded liver. *Magn Reson Imaging* 2003;**21**:519-30.

43.Storey P, Thompson AA, Carqueville CL, Wood JC, de Freitas RA, Rigsby CK. R2* imaging of transfusional iron burden at 3T and comparison with 1.5T. *J Magn Reson Imaging* 2007;**25**:540-7.

44.Spincemaille P, Anderson J, Wu G, Yang B, Fung M, Li K, et al. Quantitative Susceptibility Mapping: MRI at 7T versus 3T. *J Neuroimaging* 2020;**30**:65-75.

45.Amstad E, Textor M, Reimhult E. Stabilization and functionalization of iron oxide nanoparticles for biomedical applications. *Nanoscale* 2011;**3**:2819-43.

46.Oh JY, Kim HS, Palanikumar L, Go EM, Jana B, Park SA, et al. Cloaking nanoparticles with protein corona shield for targeted drug delivery. *Nat Commun* 2018;**9**:4548.

47.Ben Jemaa A, Sallami S, Ceraline J, Oueslati R. A novel regulation of PSMA and PSA expression by Q640X AR in 22Rv1 and LNCaP prostate cancer cells. *Cell Biol Int* 2013;**37**:464-70.

48.Tyulkina DV, Pleshkan VV, Alekseenko IV, Kopantseva MR, Sverdlov ED. Expression of the FAP gene in non-fibroblast human cell lines. Development of cancer-associated fibroblast models. *Dokl Biochem Biophys* 2016;**470**:319-21.

49.Wysock JS, Lepor H. Multi-parametric MRI imaging of the prostate-implications for focal therapy. *Transl Androl Urol* 2017;**6**:453-63.

50.Tao L, Huang G, Song H, Chen Y, Chen L. Cancer associated fibroblasts: An essential role in the tumor microenvironment. *Oncol Lett* 2017;**14**:2611-20.

51.Du H, Che G. Genetic alterations and epigenetic alterations of cancer-associated fibroblasts. *Oncol Lett* 2017;**13**:3-12.

52.Stefan AK, Katharina S, Clemens K, Erik W, Matthias FH, Sonja K, et al. Clinical outcome of PSMA-guided radiotherapy for patients with oligorecurrent prostate cancer. *Eur J Nucl Med Mol Imaging* 2021;**48**:143-51.

53.Mazzola R, Cuccia F, Figlia V, Rigo M, Nicosia L, Giaj-Levra N, et al. Stereotactic body radiotherapy for oligometastatic castration sensitive prostate cancer using 1.5 T MRI-Linac: preliminary data on feasibility and acute patient-reported outcomes. *Radiol Med* 2021;**126**:989-97.

54.Serfling SE, Hartrampf PE, Zhi Y, Higuchi T, Rowe SP, Bundschuh L, et al. Interobserver Agreement Rates on Fibroblast Activation Protein Inhibitor-Directed Molecular Imaging and Therapy. *Clin Nucl Med* 2022.

808 55.De Felice F, Piccioli A, Musio D, Tombolini V. The role of radiation therapy in bone
809 metastases management. *Oncotarget* 2017;**8**:25691-9.

810 56.Isik EG, Has-Simsek D, Sanli O, Sanli Y, Kuyumcu S. Fibroblast Activation Protein-Targeted
811 PET Imaging of Metastatic Castration-Resistant Prostate Cancer Compared With 68Ga-PSMA
812 and 18F-FDG PET/CT. *Clin Nucl Med* 2022;**47**:e54-e5.

813 57.Vaz S, Hadaschik B, Gabriel M, Herrmann K, Eiber M, Costa D. Influence of androgen
814 deprivation therapy on PSMA expression and PSMA-ligand PET imaging of prostate cancer
815 patients. *Eur J Nucl Med Mol Imaging* 2020;**47**:9-15.

816 58.Otazo R, Lambin P, Pignol JP, Ladd ME, Schlemmer HP, Baumann M, et al. MRI-guided
817 Radiation Therapy: An Emerging Paradigm in Adaptive Radiation Oncology. *Radiology*
818 2021;**298**:248-60.

819 59.Sonn GA, Fan RE, Ghanouni P, Wang NN, Brooks JD, Loening AM, et al. Prostate Magnetic
820 Resonance Imaging Interpretation Varies Substantially Across Radiologists. *Eur Urol Focus*
821 2019;**5**:592-9.

822 60.Priester A, Natarajan S, Khoshnoodi P, Margolis DJ, Raman SS, Reiter RE, et al. Magnetic
823 Resonance Imaging Underestimation of Prostate Cancer Geometry: Use of Patient Specific
824 Molds to Correlate Images with Whole Mount Pathology. *J Urol* 2017;**197**:320-6.

825 61.Hectors SJ, Semaan S, Song C, Lewis S, Haines GK, Tewari A, et al. Advanced Diffusion-
826 weighted Imaging Modeling for Prostate Cancer Characterization: Correlation with
827 Quantitative Histopathologic Tumor Tissue Composition-A Hypothesis-generating Study.
828 *Radiology* 2018;**286**:918-28.

829 62.Brennen WN, Rosen DM, Wang H, Isaacs JT, Denmeade SR. Targeting carcinoma-
830 associated fibroblasts within the tumor stroma with a fibroblast activation protein-activated
831 prodrug. *J Natl Cancer Inst* 2012;**104**:1320-34.

832 63.Liu W, Zhu Y, Ye L, Zhu Y, Wang Y. Comparison of tumor angiogenesis in subcutaneous and
833 orthotopic LNCaP mouse models using contrast-enhanced ultrasound imaging. *Transl Cancer*
834 *Res* 2021;**10**:3268-77.

835 64.Sindhwani S, Syed AM, Ngai J, Kingston BR, Maiorino L, Rothschild J, et al. The entry of
836 nanoparticles into solid tumours. *Nat Mater* 2020;**19**:566-75.

837 65.Subhan MA, Yalamarty SSK, Filipczak N, Parveen F, Torchilin VP. Recent Advances in Tumor
838 Targeting via EPR Effect for Cancer Treatment. *J Pers Med* 2021;**11**.

839 66.Hoffmann A, Oborn B, Moteabbed M, Yan S, Bortfeld T, Knopf A, et al. MR-guided proton
840 therapy: a review and a preview. *Radiat Oncol* 2020;**15**:129.

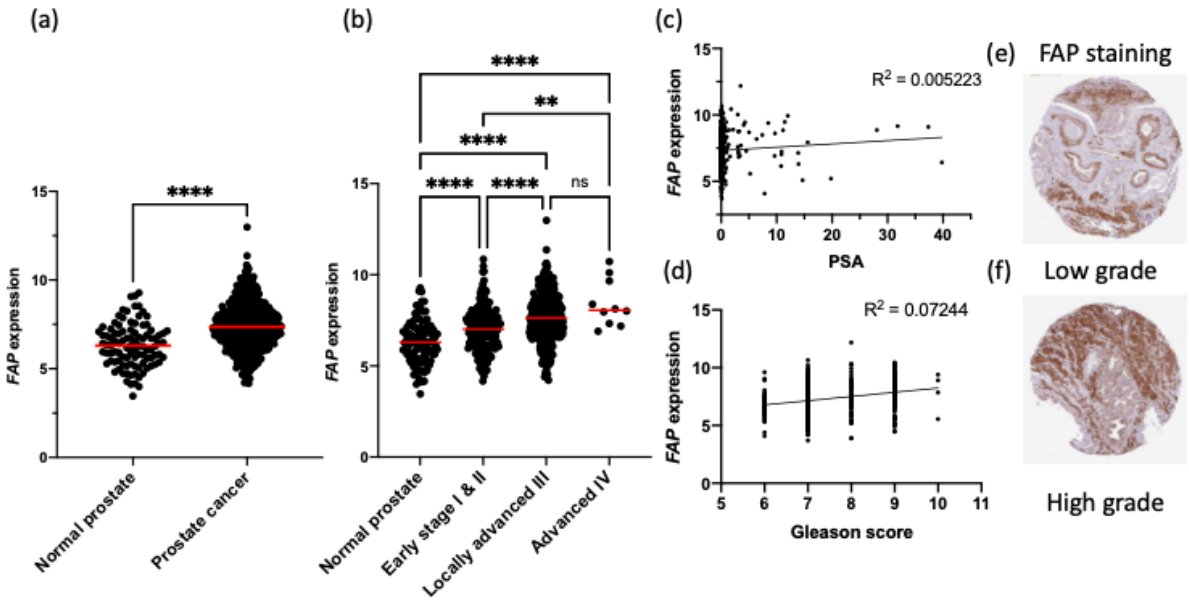

Figure 1. Transcriptomic analysis of *FAP* expression in clinical samples of prostate cancer. (a) *FAP* gene expression values in prostate tumours compared with normal prostate obtained from GTEX dataset. Red lines represent the medians of each group. (b) *FAP* expression in relation to pathological T staging, (c) PSA levels and (d) Gleason scores. (e) FAP immunohistochemistry in biopsies of low grade and (f) high grade prostate adenocarcinoma (images obtained from Human Protein Atlas).

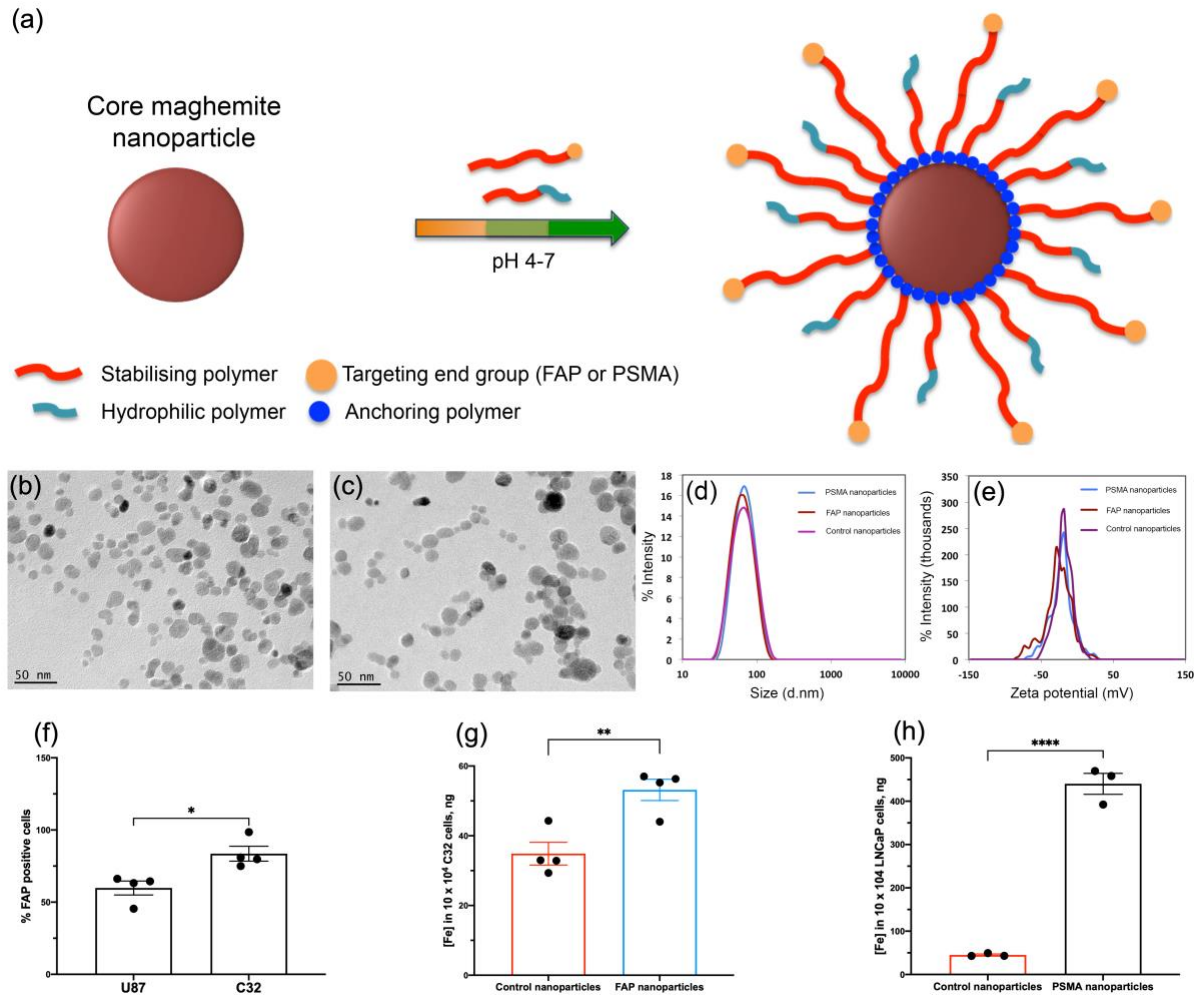

Figure 2. Preparation and characterization of FAP nanoparticles, PSMA nanoparticles and non-targeted control nanoparticles. (a) Schematic illustration of preparation of FAP/PSMA nanoparticles. (b, c) TEM images of FAP and PSMA nanoparticles at 60K x magnification. (d) Hydrodynamic size distribution by intensity and (e) zeta potentials of FAP and PSMA and unconjugated control nanoparticles measured by dynamic light scattering. Evaluation of *in vitro* binding activity to cells expressing molecular PSMA and FAP targets. (f) Flow cytometric analysis of proportion of FAP-positive U87 and C32 cells. (g) Cellular uptake of FAP nanoparticles and non-targeted nanoparticles in FAP-positive C32 cells. (h) Cellular uptake of PSMA nanoparticles and non-targeted nanoparticles in PSMA-positive LNCaP cells. Data presented as mean ± SEM from 3-4 replicates per condition. PSMA vs non-targeted nanoparticles, $p<0.0001$, $t(4)= 16.306$, FAP vs non-targeted nanoparticles, $p< 0.0001$, $t(4)= 18.892$, independent sample test.

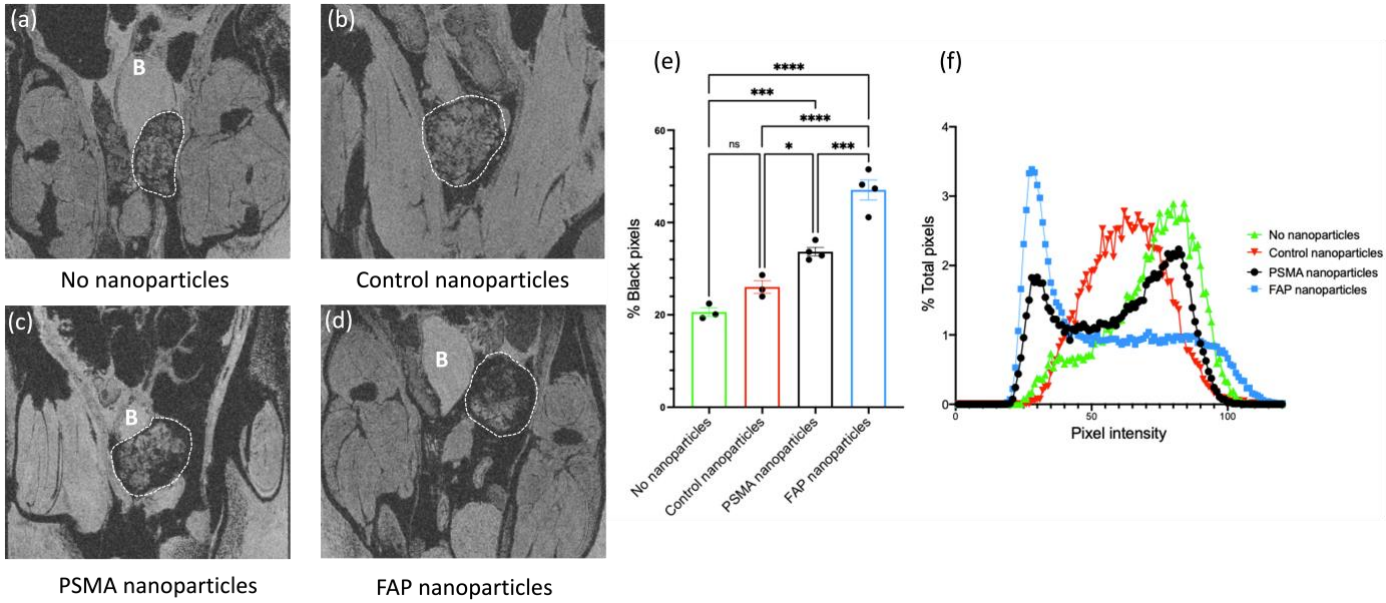

Figure 3. (a-d) Representative coronal view of the lower abdomen in whole body T_2-W 16.4T MRI of mice bearing orthotopic prostate tumours 24 hours after intravenous injection with nanoparticles (40 mg Fe/kg) (representative images). PSMA nanoparticles and FAP nanoparticles enhance tumour contrast on MRI, relative to the administration of no nanoparticles and unconjugated control nanoparticles. B indicates bladder, white dotted border indicates orthotopic prostate tumour. (e) Proportion of hypointense (black) pixels on T_2-W MRI in murine orthotopic prostate tumours 24 hours after intravenous injection of FAP and PSMA nanoparticles (data presented as mean ± SEM). (f) Representative total pixel distribution of analysed ROIs.

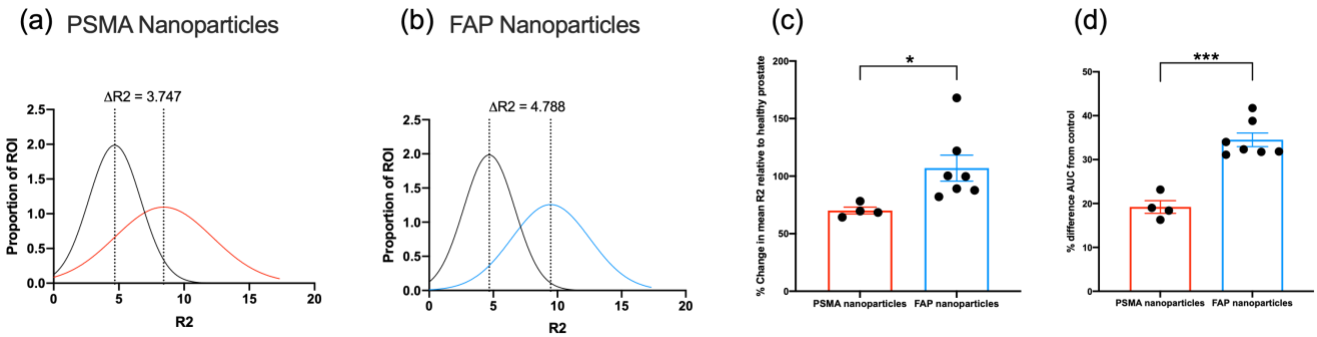

Figure 4. Assessment of change in R2 values in prostate tumours relative to healthy control prostates. Representative R2 traces of tumour borders after administration of PSMA nanoparticles (red line, a) and FAP nanoparticles (blue line, b) compared with healthy prostates (no tumour controls) with the same particles (black line). (c) Percentage change in mean R2 relative to healthy control, no tumour prostates with the same particles (70.14 vs 107.0, $p<0.05$). (d) Percentage difference of area under the curve of tumour R2 distribution curves which are not covered by the control curve (19.21% vs 34.52%, $p<0.001$).

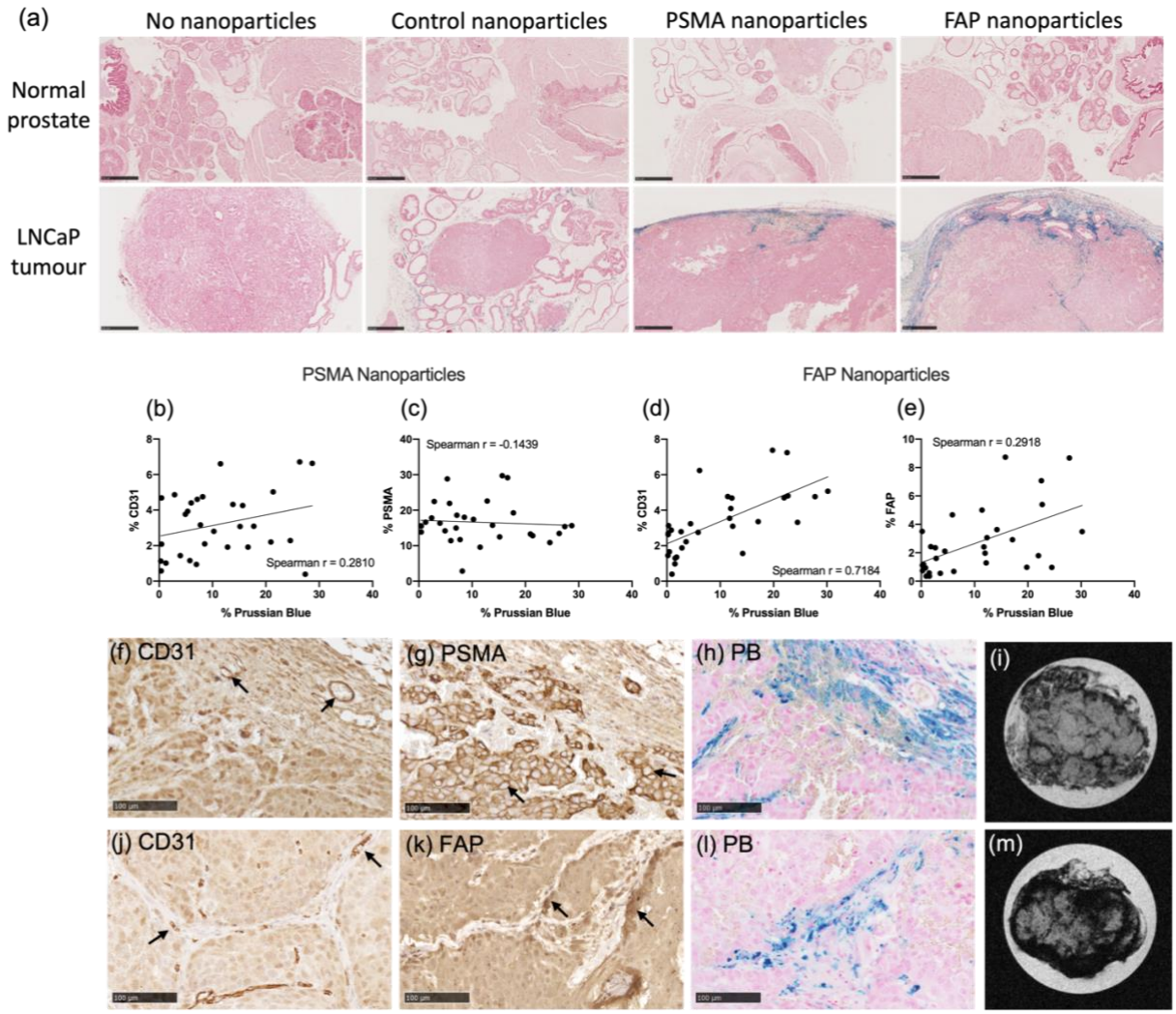

Figure 5. (a) Representative images of Prussian blue staining of cross sections of normal prostates and orthotopic prostate tumours after intravenous injection with no nanoparticles, control nanoparticles, PSMA nanoparticles and FAP nanoparticles (all nanoparticles 40 mg Fe/kg). All images 5x magnification, scale bar is 500 µm. (b-e) Correlation of sequential Prussian blue staining with immunohistochemistry analysis of CD31, PSMA and FAP expression in LNCaP tumours. (b and c) show correlation of colocalization of PSMA nanoparticles with expression of CD31 and PSMA, with representative images shown (f-h). (d and e) show correlation of colocalization of FAP nanoparticles with expression of CD31 and FAP, representative images shown (j-l). Representative images are 15x magnification, scale bar is 100 µm. Arrows indicate examples of positive staining. Relationship between positive Prussian blue area and PSMA or FAP or CD31 positive area is assessed by Spearman rank correlation (shown on graph). (I and m) High resolution *ex vivo* T_2-W 11.7T MRI of murine LNCaP tumours 24 hours after intravenous injection of PSMA and FAP nanoparticles (representative images).

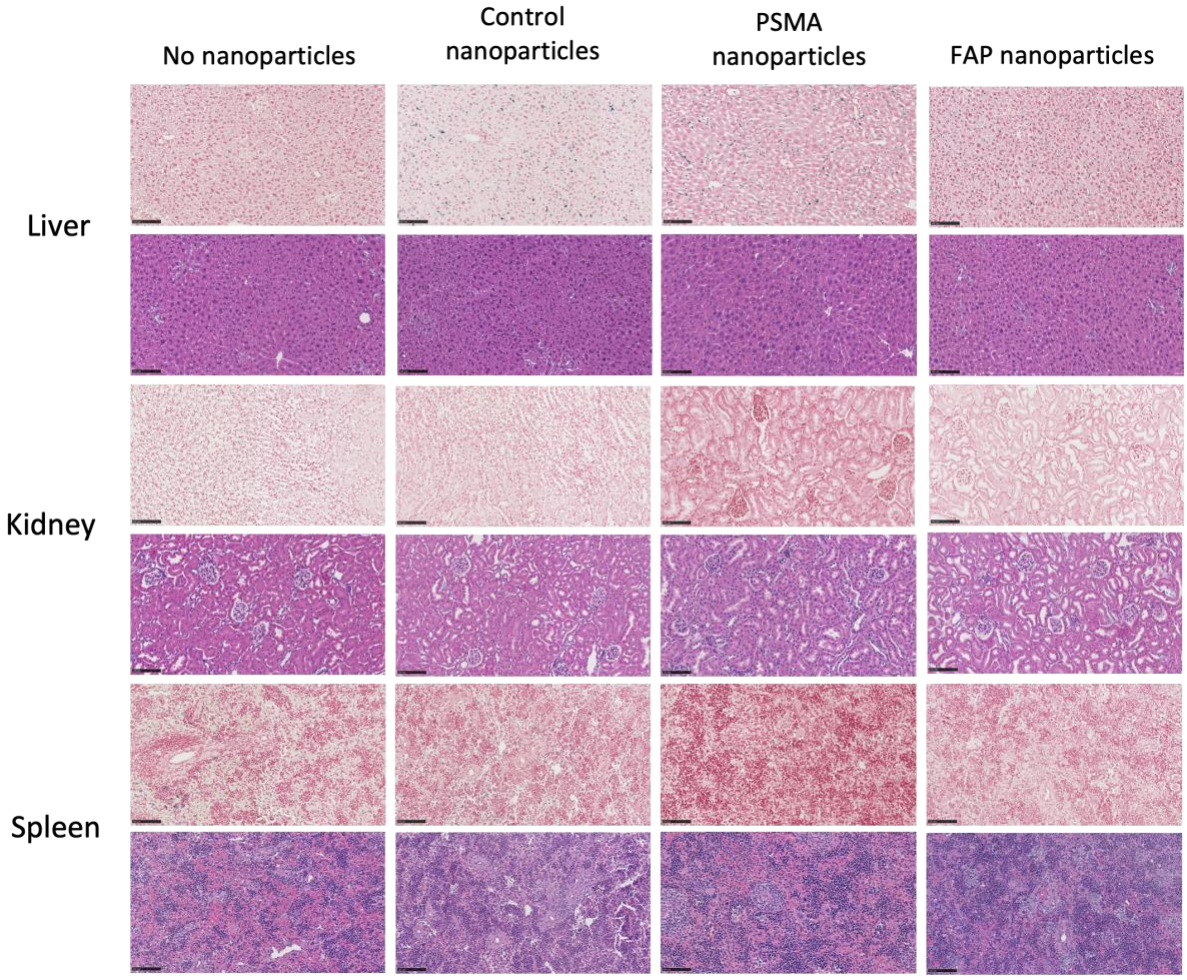

Figure 6. Haematoxylin and eosin (bottom row) and Prussian blue (top row) staining of liver, kidney and spleen of orthotopic LNCaP tumour mice, 24 hours after intravenous injection with nanoparticles. No changes in H&E staining were identified in the liver, kidney and spleen in all nanoparticle groups, compared to the no nanoparticle control. The kidneys and spleen did not show an increase in Prussian blue staining, relative to the no particle control, however a slight increase was observed in the liver, which was consistent across all nanoparticles. All images 20x magnification, scale bar is 100 µm.